Differentiation between solitary brain metastasis and glioblastoma multiforme using MRI and two-dimensional turbo spectroscopic imaging data

short title: Differentiation between solitary brain metastasis and GBM using MRI and 2D-TSI

Jan Luts [a,*], Teresa Laudadio [a,b], M. Carmen Martinez-Bisbal [c,d], Sofie Van Cauter [e], Enrique Molla [f], Jose Piquer [g], Johan A.K. Suykens [a], Uwe Himmelreich [e,h], Sabine Van Huffel [a] Bernardo Celda [c,d],

[a] *Department of Electrical Engineering (ESAT), Research Division SCD, Katholieke Universiteit Leuven, Kasteelpark Arenberg 10, B-3001 Leuven, Belgium*

[b] *Istituto Applicazioni Calcolo, CNR, sez. Bari, via G. Amendola 122/D, I-70126 Bari, Italy*

[c] *Department of Physical Chemistry, University of Valencia, C/Dr Moliner, 50, Burjassot 46100 Valencia, Spain*

[d] *Networking Research Center on Bioengineering, Biomaterials and Nanomedicine (CIBER-BBN), Valencia, Spain*

[e] *Radiology Section, University Hospitals, Katholieke Universiteit Leuven, Herestraat 49, B-3000 Leuven, Belgium*

[f] *Radiology Service, Hospital de La Ribera, Carretero Alzira-Corbera, Km 1, Alzira 46600 Valencia, Spain*

[g] *Neurosurgery Service, Hospital de La Ribera, Carretero Alzira-Corbera, Km 1, Alzira 46600 Valencia, Spain*

[h] *Department of Medical Diagnostic Sciences, Biomedical NMR Unit/MoSAIC, Katholieke Universiteit Leuven, Herestraat 49, B-3000 Leuven, Belgium*

Abstract

Brain metastases and glioblastoma multiforme represent the most aggressive and common brain tumours of the central nervous system in adults, with a completely different therapeutic approach though. Conventional magnetic resonance imaging (MRI) or clinical history, cannot always distinguish between the two types of lesion.

Therefore, this study describes the combined use of MRI and two-dimensional turbo spectroscopic imaging (2D-TSI) to differentiate glioblastomas and solitary metastases. MRI and 2D-TSI data from 10 patients (5 glioblastomas, 5 metastases) are used to compare metabolite ratios in the enhancing tumour, peri-enhancing region and the non-enhancing/non-T2 hyperintense area. It is found that the choline-to-creatine and the choline-to-N-acetylaspartate ratio are higher in the enhancing tumour and peri-enhancing region of glioblastomas compared to metastases and that both ratios allow a clear differentiation between the two tumour types. Moreover, it is shown that the infiltrative nature of glioblastomas can be visualized by an automated procedure, which also allows differentiation from metastases. This enables to generate nosologic images of the brain, offering a more realistic view of abnormal tissue regions compared to previous approaches.

Key words: brain tumour, metastasis, glioblastoma multiforme, tumour infiltration, magnetic resonance imaging (MRI), magnetic resonance spectroscopic imaging (MRSI), nosologic image

List of abbreviations

CSF (cerebrospinal fluid); Gd (gadolinium); MR (magnetic resonance); MRI (magnetic resonance imaging); MRS (magnetic resonance spectroscopy); MRSI (magnetic resonance spectroscopic imaging); TE (echo time);

* Corresponding author. Tel.: +32 16 321065; fax: +32 16 321970
Email addresses: jan.luts@esat.kuleuven.be (Jan Luts), t.laudadio@ba.iac.cnr.it (Teresa Laudadio), carmen.martinez-bisbal@uv.es (M. Carmen Martinez-Bisbal), sofie.vancauter@uz.kuleuven.ac.be (Sofie Van Cauter), enrique.molla@uv.es (Enrique Molla), jpiquer@hospital-ribera.com (Jose Piquer), johan.suykens@esat.kuleuven.be (Johan A.K. Suykens), uwe.himmelreich@med.kuleuven.be (Uwe Himmelreich), sabine.vanhuffel@esat.kuleuven.be (Sabine Van Huffel), bernardo.celda@uv.es (Bernardo Celda).

Introduction

Nowadays, magnetic resonance imaging (MRI) is widely applied in medicine as a non-invasive diagnostic tool to detect and diagnose brain disease. However, the ability to differentiate between tumour types is still limited and, a biopsy is often required for an adequate diagnosis and therapy planning. In this context, an important example is represented by brain metastasis and glioblastoma multiforme, which are the most common brain neoplasms in adults. Clinical history and the number of lesions are two important factors to distinguish metastases from glioblastomas. Although, solitary brain metastases and glioblastomas are sometimes difficult to differentiate on conventional MRI, they require different treatments.

Magnetic resonance spectroscopy (MRS) has already been used in a pattern recognition setting to differentiate glioblastomas from metastases (1–3). This technique, which is complementary to conventional MRI, provides important metabolic information on the lesion tissues and, by studying the alterations in metabolite concentrations, one can better understand the underlying pathology. However, single-voxel approaches, including short or long echo time (TE) data, did not provide a reliable differentiation between the two tumour types. The area under the receiver operating characteristic curve was 0.60 in (1), 0.64 in (2) and the accuracy was 78 % in (3). Opstad et al. obtained a more satisfactory (sensitivity = 80 %, specificity = 80 %) differentiation by considering the lipid peak area ratio (i.e. the total peak area at 1.3 ppm compared to 0.9 ppm), while no significant differences were found in the individual metabolite or lipid concentrations between the groups (4). Ishimaru et al. found that the absence of creatine in the tumoural area most likely indicates metastasis (5). Other

studies investigated the area surrounding the enhancing region in glioblastoma since these tumours diffusely infiltrate into the normal brain parenchyma. This is not observed in metastases. Infiltrated non-enhancing/non-T2 hyperintense areas, with abnormal choline-to-N-acetylaspartate ratios were reported for gliomas (6). As such, Fan et al. used single-voxel MRS to analyze MR spectra in these regions and found that choline was elevated in both the tumoural and the surrounding region for gliomas. Also, elevated myo-inositol levels were reported within the enhancing foci of gliomas (7).

Magnetic resonance spectroscopic imaging (MRSI) is able to provide metabolite maps of the brain, enabling to visualize the spatial distribution of the metabolites. Law et al. found an elevated choline-to-creatine ratio in the enhancing tumour and the peri-enhanced region in glioblastomas compared to metastases using MRSI. No differences were obtained for the N-acetylaspartate-to-creatine ratio between both tumour groups. The conclusion of that study was that MRSI can be used to distinguish between glioblastomas and metastases (8). In addition, Chiang et al. also reported a significantly higher choline-to-creatine ratio in the peri-enhancing area of glioblastomas compared to metastases, which allowed a differential diagnosis between the two tumour types. On the contrary, no statistical differences were found in the enhancing tumour region for the choline-to-creatine ratio (9).

In this study, we further investigate the differentiation between glioblastomas and metastases using MRSI and MRI information. More specifically, two-dimensional turbo spectroscopic imaging (2D-TSI) data, T1-weighted images before and after gadolinium (Gd) administration and T2-weighted images are used. 2D-TSI data are characterized by reduced acquisition times compared to those required for standard MRSI (10). The choline-to-creatine and choline-to-

N-acetylaspartate ratios for glioblastomas and metastases are compared in the enhancing tumour, the peri-enhancing area and the non-enhancing/non-T2 hyperintense region. The infiltration of glioblastomas in the non-enhancing/non-T2 hyperintense area is detected. The information is included in a nosologic image, which illustrates the ability to generate more realistic abnormal tissue areas compared to previous approaches.

Experimental

Patients

Data from ten patients with a brain tumour were considered for this study (7 men, 3 women; patient age 46-71; mean age 57.6 years). Five patients were diagnosed with a glioblastoma tumour and five with a solitary metastasis tumour (primary tumour location: colon, lung, breast, and two unknown), all confirmed by histology (Table 1). Data were acquired at the Radiology Service of Clinica Quirón, Valencia, and the Hospital de La Ribera, Alzira (Spain), as part of the routine clinical preoperative magnetic resonance (MR) imaging and spectroscopy protocol, before biopsy or surgical resection. All patients signed informed consent, in agreement with the guidelines of the University Hospital Ethical Committee.

MRI/MRSI-data acquisition

Data were acquired in 1.5 T Philips Achieva scanners (Philips Medical Systems, The Netherlands). T1-weighted images (slice thickness = 5 mm, matrix

size = 256 × 256) before and after Gd injection were acquired prior to the 2D-TSI study. A T2-weighted image package, with the same field-of-view and orientation in plane location of the 2D-TSI slice, was acquired before 2D-TSI. Image registration was performed based on the algorithm described in (11). 2D-TSI (including water-suppressed and -unsuppressed MR spectra) were acquired using a 90° - 180° - 180° pulse sequence. The multivoxel spectroscopic images consisted of a grid of 24 × 24 voxels with a field-of-view of 230 × 230 mm and a slice thickness of 20 mm. Each volume unit dimension was 9.6 × 9.6 × 20 mm (1.8 ml). 2D-TSI data were acquired with long TE (272 ms) and TR = 2000 ms. 256 complex data points were acquired and zero filled to 512 points. Data processing included eddy current correction, frequency alignment and removal of the residual water resonance by using HLSVD-PRO (12). Magnitude MR spectra were computed and peak integration was used to calculate an estimate of the concentration of choline (3.1-3.3 ppm), creatine (2.9-3.1 ppm) and N-acetylaspartate (1.9-2.1 ppm).

Choline-to-creatine and choline-to-N-acetylaspartate ratios were computed by dividing the metabolite integrals in the same MR spectrum. In addition for each patient, the choline-to-creatine and choline-to-N-acetylaspartate ratios belonging to the voxels of the enhancing tumour, peri-enhancing area (i.e. hyperintense on T2-weighted images, but not enhancing on post-Gd T1-weighted images) and the non-enhancing/non-T2 hyperintense region were averaged within each of those regions. Afterwards, these values were compared in order to differentiate the types of tumour under investigation.

Threshold method

The method by Otsu was applied to the choline-to-N-acetylaspartate map of each patient (13). This automatic method calculated an optimal threshold, such that voxels with abnormal ratios were separated from voxels with normal ratios. The goal of the method is to find a threshold that minimizes the within-class variance, which has been shown to be equivalent to maximizing the between-class variance. Using σ_T^2 for the total variance and σ_B^2 for the between-class variance, the following function is maximized:

$$t^* = arg \max_t \frac{\sigma_B^2}{\sigma_T^2}, \tag{1}$$

where t^* is the optimal threshold. Once t^* is fixed, the final output of the threshold method is a binary map, indicating voxels with normal and abnormal choline-to-N-acetylaspartate ratios. Otsu threshold selection is an efficient method due to its recursive nature.

Nosologic images

A nosologic image summarizes the presence of different tissues and lesions in a single image by color coding each voxel according to the tissue type it is assigned to (14). In (15), a nosologic imaging technique was proposed combining methods from image processing as well as pattern recognition to segment and classify brain tumours based on MRI and MRSI data. First, a registered digital brain atlas and a subject-specific abnormal tissue prior, obtained from MRSI data, were used for the segmentation of the MRI data. Next, the de-

tected abnormal tissue was classified based on supervised pattern recognition of the spectroscopic data. In the present study, we also generated nosologic images, but, only the output from the first step (i.e. segmentation of MRI) of the nosologic imaging method was used. The actual segmentation procedure consisted of two stages: detection of abnormal tissue and reclassification with spatial and geometric constraints (Algorithm 1).

Abnormal tissue was detected using an iterative procedure by first using a threshold on the posterior probabilities, or atlas probabilities in the first iteration. In this way, pixels in high confidence regions were sampled. Next, the minimum covariance determinant estimator was used to remove samples from normal tissue that exceeded a distance threshold (16), after which a non-parametric model was used to estimate the probability density functions from the obtained samples. The subject-specific atlas priors were updated with the estimated densities to compute the posterior probabilities. Finally, a bias field correction, which was estimated from the white and gray matter probabilities, was performed to compensate for image inhomogeneity. The second stage of the segmentation procedure was iterative too and focussed on reclassification with spatial and geometric constraints by means of region competition snakes (17). First, a threshold was used on the posterior probabilities and a sampling was performed. Abnormal tissue samples were pruned based on the level-set evolution after which the densities were estimated. The second stage ended with the calculation of the posterior class probabilities and inclusion of a bias field correction. As a result, the segmentation step, including the two stages, produced a segmented MR image that separated abnormal tissue from gray matter, white matter and cerebrospinal fluid (CSF) (15).

In the present study, we applied the segmentation step to the T2-weighted MR

Algorithm 1. MRI segmentation

1: {Detection of abnormality}
2: **loop**
3: Threshold posterior (or atlas probabilities in first iteration) probabilities to sample from high confidence regions
4: Outlier detection based on minimum covariance determinant estimator to remove samples from normal tissue
5: Compute probability density functions for all tissue classes using a non-parametric model (i.e. kernel expansions)
6: Apply Bayes' rule to calculate posterior probabilities
7: Perform bias field correction
8: **end loop**
9: {Reclassification with spatial and geometric constraints}
10: **loop**
11: Threshold posterior probabilities to sample from high confidence regions
12: Tumour samples are pruned using region competition snakes.
13: Compute probability density functions for all tissue classes using a non-parametric model (i.e. kernel expansions)
14: Apply Bayes' rule to calculate posterior probabilities
15: Perform bias field correction
16: **end loop**

images such that the segmented abnormal region matched with the T2 hyper-intense region. Next, the binary map, obtained by applying Otsu's threshold method to the choline-to-N-acetylaspartate ratio estimated from the 2D-TSI data, was superimposed to the segmented abnormal region. Abnormal voxels of the binary map which fell outside the lesion obtained by the segmentation step, corresponded to infiltration.

Results

In vivo MR studies were carried out on ten patients, five patients with glioblastoma and five with metastatic disease. The results are presented in three steps. First, we demonstrate distinct differences in metabolites ratios in glioblastomas and metastases, allowing differentiation. Next, the infiltrative nature of

the glioblastoma tumour is detected and, finally, this information is visualized in a nosologic image.

Metabolite ratios

For each patient, the voxels were divided into three groups: enhancing tumour, peri-enhancing area (i.e. hyperintense on T2-weighted images, non-enhancing on post-Gd T1-weighted images) and the non-enhancing/non-T2 hyperintense region. Within each group, the choline-to-creatine and choline-to-N-acetylaspartate ratio were averaged per patient (Table 2).

Table 2 summarizes the choline-to-creatine ratios, which were averaged over all patients with the same type of tumour, for the three regions. The averaged($\pm$ standard deviation) choline-to-creatine ratio in the non-enhancing/non-T2 hyperintense area of glioblastomas was 1.42 ± 0.19 compared to 1.28 ± 0.18 in metastases. In the peri-enhancing area the ratio was 2.02 ± 0.73 in glioblastomas and 1.18 ± 0.15 in metastases, while ratios equal to 3.13 ± 1.22 and 1.80 ± 0.24 were observed in the enhancing tumour of glioblastomas and metastases, respectively. As such, a clear difference in choline-to-creatine was found in the peri-enhancing and the enhancing tumour between glioblastomas and metastases. In addition, the difference between the averaged ratio from the enhancing tumour and the non-enhancing/non-T2 hyperintense area was calculated for each patient and a clear separation between metastases and glioblastomas was obtained (Figure 1).

Similarly, Table 2 provides the choline-to-N-acetylaspartate ratios, averaged over all patients within the same tumour class, for the three regions. The averaged($\pm$ standard deviation) choline-to-N-acetylaspartate ratio was 0.48 ± 0.06

in the non-enhancing/non-T2 hyperintense area of glioblastomas, compared to 0.43±0.08 in metastases. The ratio was 1.08±0.89 in the peri-enhancing area of glioblastomas and 0.54±0.08 in metastases. For the enhancing tumour of glioblastomas the ratio value was 2.39±2.05, while 0.97±0.13 was found for metastases. The choline-to-N-acetylaspartate ratio in the peri-enhancing and the enhancing tumour was different in glioblastomas and metastases. Finally, also in this case, the difference between the averaged ratio from the enhancing tumour and the non-enhancing/non-T2 hyperintense area allowed a clear differentiation between metastases and glioblastomas (Figure 1).

Infiltration

The region where the glioblastoma tumour infiltrated normal appearing tissue, was indicated on the MRI. Otsu's threshold selection was applied to the choline-to-N-acetylaspartate values of a patient to generate a binary map, indicating voxels with normal and abnormal ratios. The output of the threshold selection was superimposed on the T2-weighted MR images, included in the 2D-TSI slice, for two patients with glioblastoma (Figures 2 - 3) and for two patients with metastatic disease (Figures 4 - 5). Voxels with abnormal choline-to-N-acetylaspartate values were indicated in red, while normal ones are indicated in blue.

Case 3 represents a patient with a glioblastoma, as assigned by the pathologists, having a satellite lesion (Figure 2). Voxels with abnormal choline-to-N-acetylaspartate values were found in the T2 hyperintense lesion, as well as in adjacent tissue in the contralateral hemisphere. MR spectrum (a) in Figure 2 clearly shows increased choline compared to N-acetylaspartate and creatine.

The voxel is situated outside the T2 hyperintense region, suggesting that it corresponds to infiltrating glioblastoma. MR spectra from normal tissue (spectrum (b)) and the enhancing tumour area (spectrum (c)) are also provided. Case 4 represents another patient with a glioblastoma tumour (Figure 3). The MR spectrum of voxel (b) shows that choline was increased compared to N-acetylaspartate and creatine. MR spectrum (a), originating from a voxel positioned in the normal contralateral brain and a pure tumour MR spectrum (c) are also depicted.

Case 6 is a patient with metastatic disease, showing no infiltration in the adjacent brain parenchyma (Figure 4). The voxels with abnormal choline-to-N-acetylaspartate completely corresponded to the hyperintense area on the T2-weighted MR images. MR spectra from different locations are displayed, showing nearly equivalent levels of choline and creatine and increased N-acetylaspartate. These voxels are located outside the tumoural lesion, in peri-enhancing edema or in normal brain parenchyma. For case 10, having a metastasis, all voxels with abnormal choline-to-N-acetylaspartate levels were encapsulated in the hyperintense area on T2-weighted MR images (Figure 5). MR spectra show similar choline and creatine levels, with elevated N-acetylaspartate.

Nosologic images

The nosologic image for case 1 illustrated the infiltrative nature of a glioblastoma, with a periependimary extension (Figure 6). The abnormal tissue area, as obtained from the T2-weighted MRI, is labeled in red in the nosologic image, while voxels with abnormal choline-to-N-acetylaspartate levels that fall

outside this area are indicated in white. MR spectra (a) and (b), belonging to these white voxels in the non-enhancing/non-T2 hyperintense area at the top, are shown (Figure 6). Choline was increased with respect to N-acetylaspartate and creatine, indicating tumour infiltration. Case 2 represents a glioblastoma patient, having satellite lesions (Figure 7). The significantly broader white area, as compared to the red region, in the nosologic image suggested tumour infiltration. Green reflects CSF, light blue white matter and dark blue gray matter. MR spectrum (b), situated in the infiltrated area is visualized in Figure 7, together with MR spectra from the (enhancing) tumour (spectrum (a)) and normal tissue (spectrum (c)).

Case 9 is a patient with a metastasis tumour (Figure 8). The red region, obtained from T2-weighted MR image segmentation, shows good agreement with the voxels that had abnormal choline-to-N-acetylaspartate. MR spectra from different locations at the tumour border show similar choline and creatine peaks, while N-acetylaspartate was strongly increased. Finally, the segmented abnormal region, obtained from the T2-weighted MRI, matched with the voxels that have abnormal choline-to-N-acetylaspartate levels for case 8, a metastasis (Figure 9). MR spectra, positioned at the tumour border, corresponded to normal brain parenchyma, suggesting no tumour infiltration. The remaining white areas corresponded to voxels that partially contain abnormal tissue.

Discussion

Glioblastoma multiforme and brain metastasis are the most common brain tumours in adults. Despite major treatment advances, their prognosis remains

poor (18, 19). Glioblastoma multiforme is the most aggressive type of glioma. They arise from astrocytes, a subtype of the macroglia cells in the central nervous system. Glioblastomas are associated with dismal prognosis owing to their ability to infiltrate diffusely into the normal brain parenchyma and the complex character of the tumour itself (20). Median survival is less than one year from the time of diagnosis. Brain metastases are among the most feared complications of cancer and occur in 10-40% of all cancer patients. Among adults, the most common primary sites of brain metastases are lung cancer, breast cancer and melanoma (19, 21). Appropriate treatment choice relies on different factors including patient age, number of metastases, primary tumour type, functional status and extent of extracranial disease (21). These factors also determine prognosis. Median survival ranges from 2 to 16 months (19, 21). Therapeutic approaches for brain tumours include surgery, radiotherapy and chemotherapy (19–23). Most patients are treated with combination therapy, according to prognostic factors, tumour type and histology.

MRI is the method of choice for diagnosis, evaluation and follow-up of brain tumours (24). Glioblastomas and brain metastases usually show as irregularly shaped lesions with ring-like zones of contrast enhancement surrounding a central hypointense area of necrosis on Gd-enhanced T1-weighted images (19, 25). Differentiation between tumour types or between tumour recurrence versus therapy-related changes remains challenging. Advanced MRI techniques like MR spectroscopy, diffusion- and perfusion-weighted MRI provide new methods for the assessment of different brain pathologies (26–29).

Based on conventional MRI alone it is often difficult to differentiate between solitary metastasis and glioblastomas. Therefore, this study explored the use of additional information provided by MR spectroscopic imaging and combined it

in nosologic images. In brain tumours, the concentration of N-acetylaspartate is usually reduced since it is known to be a marker of neuronal and axonal density and viability. A decrease in N-acetylaspartate is associated with a loss of neurons or axonal injury. On the other hand, choline often shows an increased concentration in brain tumours. The resonance at 3.2 ppm is assigned to the trimethylammonium group of choline and its derivatives. The major contributors to the resonance are phosphorylcholine and glycerophosphorylcholine, while free choline is a minor component (30–32). In case of pathology, the contribution of choline increases significantly, as it reflects membrane, myelin and lipid turnover (30, 32). Creatine is essential for cell energetics and mainly originates from intracellular metabolite pools of creatine and phosphocreatine. The creatine peak at 3.0 ppm is a composite of creatine and phosphocreatine with a similar chemical shift of the CH_3-group. The 3.0 ppm peak can be reduced in some tumours (31, 33).

Previous studies, differentiating glioblastomas from metastases, applied single-voxel MR spectroscopy, which provides metabolic information from a single location in the brain in a short period of time (4, 7). In the present study, long TE 2D-TSI data were acquired to provide metabolite maps of the brain. Generally, around 6 minutes are needed to collect a 2D-TSI slice with a 24 $\times$ 24 matrix resolution (turbo factor 3), while 30 minutes are required by standard acquisition sequences with the same spatial resolution. The advantage of this multivoxel protocol is that the entire tumour, the peri-enhancing region and the non-enhancing/non-T2 hyperintense brain can be sampled rapidly with relatively high spatial resolution. In this way, the metabolically most active portion of the tumour can be identified with higher likelihood compared to single-voxel MR spectroscopy, where voxel position is essential and often

subjective.

Preul et al. averaged long TE (272 ms) 1.5 T multivoxel MR spectroscopic data within the tumour region and an elevated choline level was found in glioblastomas (24 cases) as compared to metastases (16 cases) (34). Law et al. compared the maximal choline-to-creatine ratio for high-grade gliomas (11 cases) and metastases (6 cases) in the tumoural, peri-tumoural (hyperintense on T2-weighted MRI, but non-enhancing on post-Gd T1-weighted MRI) and normal contralateral brain parenchyma using long TE (135 ms) 1.5 T MRSI (8). The choline-to-creatine ratio was 0.96±0.19 and 0.86±0.19 in the normal contralateral brain parenchyma, 2.28±1.24 and 0.76±0.23 in the peri-tumoural area, and 3.92±3.31 and 1.84±1.22 in the enhancing tumour for glioblastomas and metastases, respectively. Law et al. reported significant differences for choline-to-creatine in the enhancing tumour and peri-enhancing area. Fan et al. used short TE (45 ms) single-voxel MR spectroscopy (2.0 T) to compare maximal choline-to-creatine in similar regions in high-grade gliomas (14 cases of which 6 were glioblastoma) and metastases (8 cases) (7). Choline-to-creatine was 0.91±0.17 and 0.87±0.24 in the normal contralateral brain parenchyma, 2.65±0.32 and 1.22±0.38 in the peri-tumoural area, and 4.98±1.46 and 1.37±0.92 in the enhancing tumour for glioblastomas and metastases, respectively. Significant differences were found for choline-to-creatine in the enhancing tumour and the peri-tumoural region. Finally, Chiang et al. compared the maximal choline-to-creatine ratio using 3 T long TE (270 ms) MRSI between high-grade gliomas (14 cases) and metastases (12 cases) and only found a significant difference in the peri-tumoural area; 0.29±0.51 in metastases and 1.30±0.45 in glioblastomas (9). The ratio in the tumoural region was 1.55±0.74 and 1.82±0.66 for metastases and glioblas-

tomas, respectively.

In our study, the choline-to-creatine and choline-to-N-acetylaspartate ratio were analyzed in the enhancing tumour, the peri-enhancing area and the non-enhancing/non-T2 hyperintense region. The term peri-enhancing was preferred over peri-tumoural, since the margin of a high-grade glioma is not defined by a T2-weighted MRI because of the highly infiltrative nature of glioma (8, 20). Ratios from the voxels were averaged within each of the regions. Differences in averaged choline-to-creatine and averaged choline-to-N-acetylaspartate were found in the enhancing tumour and peri-enhancing area between glioblastomas and metastases. The present study does not indicate a preferred ratio for discrimination. We would rather advise to combine both ratios to extract a decision rule. Although a limited number of patients has been used in this study, these findings are consistent with what has already been published in the literature, supporting our conclusions. The ratios Law et al. reported for choline-to-creatine are, relatively with respect to each other, identical to the values in the present study. The ranking of the choline-to-creatine ratio values for glioblastomas and metastases in the three regions under investigation, is exactly the same as in the present study. Compared to the previous approaches, this study also focusses on the visualization of tumour infiltration.

Although the comparison between metabolite ratios in the tumour and peri-enhancing region allows clear differentiation between glioblastomas and metastases, it does not directly show where the potential infiltration is situated. Therefore, infiltration is automatically detected and visualized using colored maps and nosologic images in this study. A nosologic image offers an interesting way to represent tumour heterogeneity, which may help clinicians in

making therapeutic decisions. However, a limitation of our previous nosologic imaging approach, was that only MR spectroscopic information within the MRI-based lesions were considered. As such, the resulting nosologic image showed a tumour contour that was similar to the one that can be observed on the MR image (15). This is not what can be expected in case of diffuse infiltrative tumours (e.g. glioma (20)). In the present study, the colored maps, calculated from choline-to-N-acetylaspartate, were superimposed to the nosologic images to visualize infiltration. Choline-to-N-acetylaspartate and N-acetylaspartate are known to be important markers for tumour infiltration in gliomas (35). MR spectra with an abnormal choline-to-N-acetylaspartate ratio have been found in the peri-enhancing and non-enhancing/non-T2 hyperintense region of gliomas, and, in addition, a negative correlation between the N-acetylaspartate level and the degree of tumour infiltration has been reported (6, 36, 37). The peri-enhancing region represents an increase in interstitial water due to alterations in capillary permeability and blood-brain barrier breakdown, caused by the tumour (8). In case of high-grade gliomas, this region contains tumour cell infiltration along vascular channels. In metastases, signal abnormality in the peri-enhancing region is likely due to pure vasogenic edema.

In this study, two-dimensional MR spectroscopic data were acquired with the MRSI box positioned to include maximum tumour volume to differentiate solitary metastases from glioblastoma multiforme. In future studies, the use of three-dimensional MRSI will probably increase, since it enables to cover an even larger part of the tumour (38). This technology can potentially improve the accuracy of MR spectroscopy to differentiate metastases from glioblastomas based on the entire tumour volume. Furthermore, various researchers

proposed to use other methods like diffusion-weighted MRI, diffusion tensor imaging and perfusion-weighted MRI. The combination of those methods with MRSI may further improve their diagnostic potential (8, 9, 39–45).

Conclusions

This paper illustrates the combined use of 2D-TSI and MRI data to differentiate glioblastoma multiforme from solitary metastases by means of two approaches. First, it is shown that the choline-to-creatine and choline-to-N-acetylaspartate ratios are significantly different for glioblastomas compared to metastases in the enhancing tumour and the peri-enhancing area. The calculated difference between the ratio in the enhancing tumour and the ratio in the non-enhancing/non-T2 hyperintense region is larger for glioblastomas compared to metastases, such that a differentiation between the two tumour types can be made. The infiltrative nature of glioblastomas into the normal/surrounding/adjacent brain parenchyma, is detected, allowing a further differentiation between both types of tumour. Finally, it is shown that the abnormal tissue area of nosologic images can be improved based on this new approach. The combination of the results, described in this paper, suggests that MRI and 2D-TSI are able to demonstrate the differences between glioblastomas and metastases, which can potentially lead to further therapeutic optimization in the future.

Acknowledgements

This research is funded by a PhD grant of the Institute for the Promotion of Innovation through Science and Technology in Flanders (IWT-Vlaanderen); The work of TL is supported by the Short-Term Mobility Program 2008 of the National Research Council of Italy; Research supported by Research Council KUL: GOA-AMBioRICS, several PhD/postdoc & fellow grants, Center Of Excellence Optimisation, IDO 05/010 EEG-fMRI, GOA/2004/05 (Mixing and Analyzing Real and Virtual Environments and Lighting); FWO: PhD/postdoc grants, projects, G.0360.05 (Advanced EEG analysis techniques for epilepsy monitoring), G.0519.06 (Noninvasive brain oxygenation), G.0341.07 (Data fusion), G.0321.06 (Numerical tensor techniques for spectral analysis), G.0302.07 (Support vector machines and kernel methods), G.0566.06 (Computational strategies for shape modeling and matching and their application in medical image analysis), research communities (ICCoS, ANMMM), UH acknowledges the support by the K.U. Leuven Center Of Excellence 'MoSAIC'; The Biomedical Informatics Group (IBIME, ITACA Institute) of the Technical University of Valencia is gratefully acknowledged; The Medical Imaging Center of the Katholieke Universiteit Leuven is gratefully acknowledged; Ministerio de Educación y Ciencia del Gobierno de España (SAF2007-6547, SAF2007-29455-E, SAF2007-29394-E, SAF2007-29393-E); IWT: PhD Grants; Belgian Federal Government: DWTC (IUAP IV-02 (1996-2001), IUAP V-22 (2002-2006): Dynamical Systems and Control: Computation, Identification & Modelling) and Belgian Federal Science Policy Office IUAP P6/04 (Dynamical systems, control and optimization, 2007-2011); EU: eTUMOUR (contract no. FP6-2002-LIFESCIHEALTH 503094), HealthAgents (contract no. FP6-2005-IST 027213), FAST (contract no. FP6-019279-2), ESA: Cardiovascular Control (Prodex-8 C90242).

References

[1] Devos A, Lukas L, Suykens JAK, Vanhamme L, Tate AR, Howe FA, Majos C, Moreno-Torres A, van der Graaf M, Arus C, Van Huffel S, Classification of brain tumours using short echo time 1H MR spectra. *Journal of Magnetic Resonance.* 2004; **170**: 164–175.

[2] Lukas L, Devos A, Suykens JAK, Vanhamme L, Howe FA, Majos C, Moreno-Torres A, van der Graaf M, Tate AR, Arus C, Van Huffel S, Brain tumor classification based on long echo proton MRS signals. *Artificial Intelligence in Medicine.* 2004; **31**: 73–89.

[3] Garcia-Gomez JM, Luts J, Julia-Sape M, Krooshof P, Tortajada S, Vicente Robledo J, Melssen W, Fuster-Garcia E, Olier I, Postma G, Monleon D, Moreno-Torres A, Pujol J, Candiota A-P, Martinez-Bisbal MC, Suykens JAK, Buydens L, Celda B, Van Huffel S, Arus C, Robles M, Multiproject-multicenter evaluation of automatic brain tumor classification by magnetic resonance spectroscopy. *Magnetic Resonance Materials in Physics, Biology and Medicine.* 2009; **22**: 5–18.

[4] Opstad KS, Murphy MM, Wilkins PR, Bell BA, Griffiths JR, Howe FA, Differentiation of metastases from high-grade gliomas using short echo time 1H spectroscopy. *Journal of Magnetic Resonance Imaging.* 2004; **20**: 187–192.

[5] Ishimaru H, Morikawa M, Iwanaga S, Kaminogo M, Ochi M, Hayashi K, Differentiation between high-grade glioma and metastatic brain tumor using single-voxel proton MR spectroscopy. *European Radiology.* 2001; **9**: 1784–1791.

[6] Di Costanzo A, Scarabino T, Trojsi F, Popolizio T, Catapano D, Giannatempo GM, Bonavita S, Portaluri M, Tosetti M, d'Angelo VA, Salvolini

U, Tedeschi G, Proton MR spectroscopy of cerebral gliomas at 3T: spatial heterogeneity, and tumor grade and extent. *European Radiology.* 2008; **18**: 1727–1735.

[7] Fan G, Sun B, Wu Z, Guo Q, Guo Y, In vivo single-voxel proton MR spectroscopy in the differentiation of high-grade gliomas and solitary metastases. *Clinical Radiology.* 2004; **59**: 77–85.

[8] Law M, Cha S, Knopp EA, Johnson G, Arnett J, Litt AW, High-grade gliomas and solitary metastases: differentiation by using perfusion and proton spectroscopic MR imaging. *Radiology.* 2002; **222**: 715–721.

[9] Chiang IC, Kuo Y-T, Lu C-Y, Yeung K-W, Lin W-C, Sheu F-O, Liu G-C, Distinction between high-grade gliomas and solitary metastases using peritumoral 3-T magnetic resonance spectroscopy, diffusion, and perfusion imagings. *Neuroradiology.* 2004; **46**: 619–627.

[10] Duyn J, Moonen C, Fast proton spectroscopic imaging of human brain using multiple spin-echoes. *Magnetic Resonance in Medicine.* 1993; **30**: 409–414.

[11] Maes F, Collignon A, Vandermeulen D, Marchal G, Suetens P, Multimodality image registration by maximization of mutual information. *IEEE Transactions on Medical Imaging.* 1997; **16**: 187–198.

[12] Laudadio T, Mastronardi N, Vanhamme L, Van Hecke P, Van Huffel S, Improved Lanczos algorithms for blackbox MRS data quantitation. *Journal of Magnetic Resonance.* 2002; **157**: 292–297.

[13] Otsu N, A threshold selection method from gray-level histograms. *IEEE Transactions on Systems, Man and Cybernetics.* 1979; **9**: 62–66.

[14] Szabo de Edelenyi F, Rubin C, Esteve F, Grand S, Decorps M, Lefournier V, Le Bas JF, Remy C, A new approach for analyzing proton magnetic resonance spectroscopic images of brain tumors: nosologic images. *Nature*

Medicine. 2000; **6**: 1287–1289.

[15] Luts J, Laudadio T, Idema AJ, Simonetti AW, Heerschap A, Vandermeulen D, Suykens JAK, Van Huffel S, Nosologic imaging of the brain: segmentation and classification using MRI and MRSI. *Accepted for publication in Nuclear Magnetic Resonance in Biomedicine.* 2009.

[16] Van Driessen K, Rousseeuw PJ, A fast algorithm for the minimum covariance determinant estimator. *Technometrics.* 1999; **41**: 212–223.

[17] Ho S, Bullitt E, Gerig G, Level-set evolution with region competition: Automatic 3-D segmentation of brain tumors. In *International Conference on Pattern Recognition*, IEEE Computer Society, Washington. 2002; 532–535.

[18] DeAngelis LM, Brain tumours. *The New England Journal of Medicine.* 2001; **344**: 114–123.

[19] Norden AD, Wen PY, Kesari S, Brain metastases. *Current Opinion in Neurology.* 2005; **18**: 654–661.

[20] Lefranc F, Sadeghi N, Camby I, Metens T, Dewitte O, Kiss R, Present and potential future issues in glioblastoma treatment. *Expert Review of Anticancer Therapy.* 2006; **6**: 719–732.

[21] Eichler AF, Loeffler JS, Multidisciplinary management of brain metastases. *The Oncologist.* 2007; **12**: 884–898.

[22] Stupp R, Mason WP, van den Bent MJ, Weller M, Fisher B, Taphoorn MJB, Belanger K, Brandes AA, Marosi C, Bogdahn U, Curschmann J, Janzer RC, Ludwin SK, Gorlia T, Allgeier A, Lacombe D, Cairncross JG, Eisenhauer E, Mirimanoff RO, Radiotherapy plus concomitant and adjuvant temozolomide for glioblastoma. *The New England Journal of Medicine.* 2005; **352**: 987–996.

[23] Rades D, Kueter J-D, Hornung D, Veninga T, Hanssens P, Schild SE,

Dunst J, Comparison of stereotactic radiosurgery (SRS) alone and whole brain radiotherapy (WBRT) plus a stereotactic boost (WBRT + SRS) for one to three brain metastases. *Strahlentherapie und Onkologie.* 2008; **184**: 655–662.

[24] Rees J, Advances in magnetic resonance imaging of brain tumours. *Current Opinion in Neurology.* 2003; **16**: 643–650.

[25] Schaefer PW, Budzik Jr RF, Gonzalez RG, Imaging of cerebral metastases. *Neurosurgery Clinics of North America.* 1996; **7**: 393–423.

[26] Young GS, Setayesh K, Spin-echo echo-planar perfusion MR imaging in the differential diagnosis of solitary enhancing brain lesions: distinguishing solitary metastases from primary glioma. *Accepted for publication in American Journal of Neuroradiology.* 2008.

[27] Smith EA, Carlos RC, Junck LR, Tsien CI, Elias A, Sundgren PC, Developing a clinical decision model: MR spectroscopy to differentiate between recurrent tumor and radiation change in patients with new contrast-enhancing lesions. *American Journal of Roentgenology.* 2009; **192**: W45–W52.

[28] Weber M-A, Giesel FL, Stieltjes B, MRI for identification of progression in brain tumors: from morphology to function. *Expert Review of Neurotherapeutics.* 2008; **8**: 1507–1525.

[29] Hamstra DA, Galban CJ, Meyer CR, Johnson TD, Sundgren PC, Tsien C, Lawrence TS, Junck L, Ross DJ, Rehemtulla A, Ross BD, Chenevert TL, Functional diffusion map as an early imaging biomarker for high-grade glioma: correlation with conventional radiologic response and overall survival. *Journal of Clinical Oncology.* 2008; **26**: 3387–3394.

[30] Usenius J-P, Vainio P, Hernesniemi J, Kauppinen RA, Choline-containing compounds in human astrocytomas studied by 1H NMR spectroscopy in

vivo and in vitro. *Journal of Neurochemistry.* 1994; **63**: 1538–1543.

[31] Danielsen RE, Ross B, *Magnetic resonance spectroscopy diagnosis of neurological diseases.* Marcel Dekker Inc., New York. 1999.

[32] Podo F, Tumour phospholipid metabolism. *Nuclear Magnetic Resonance in Biomedicine.* 1999; **12**: 413–439.

[33] Kinoshita Y, Yokota A, Absolute concentrations of metabolites in human brain tumors using in vitro proton magnetic resonance spectroscopy. *Nuclear Magnetic Resonance in Biomedicine.* 1997; **10**: 2–12.

[34] Preul MC, Caramanos Z, Leblanc R, Villemure JG, Arnold DL, Using pattern analysis of in vivo proton MRSI data to improve the diagnosis and surgical management of patients with brain tumors. *Nuclear Magnetic Resonance in Biomedicine.* 1998; **11**: 192–200.

[35] Ganslandt O, Stadlbauer A, Fahlbusch R, Kamada K, Buslei R, Blumcke I, Moser E, Nimsky C, Proton magnetic resonance spectroscopic imaging integrated into image-guided surgery: correlation to standard magnetic resonance imaging and tumor cell density. *Neurosurgery.* 2005; **56**: 291–298.

[36] Croteau D, Scarpace L, Hearshen D, Gutierrez J, Fisher JL, Rock JP, Mikkelsen T, Correlation between magnetic resonance spectroscopy imaging and image-guided biopsies: Semiquantitative and qualitative histopathological analyses of patients with untreated glioma. *Neurosurgery.* 2001; **49**: 823–829.

[37] Stadlbauer A, Gruber S, Nimsky C, Fahlbusch R, Hammen T, Buslei R, Tomandl B, Moser E, Ganslandt O, Preoperative grading of gliomas by using metabolite quantification with high-spatial-resolution proton MR spectroscopic imaging. *Radiology.* 2006; **238**: 958–969.

[38] Osorio JA, Ozturk-Isik E, Xu D, Cha S, Chang S, Berger MS, Vigneron

DB, Nelson SJ, 3D 1H MRSI of brain tumors at 3.0 tesla using an eight-channel phased-array head coil. *Journal of Magnetic Resonance Imaging.* 2007; **26**: 23–30.

[39] Law M, Yang S, Wang H, Babb JS, Johnson G, Cha S, Knopp EA, Zagzag D, Glioma grading: Sensitivity, specificity, and predictive values of perfusion MR imaging and proton MR spectroscopic imaging compared with conventional MR imaging. *American Journal of Neuroradiology.* 2003; **24**: 1989–1998.

[40] Tsuchiya K, Fujikawa A, Nakajima M, Honya K, Differentiation between solitary brain metastasis and high-grade glioma by diffusion tensor imaging. *British Journal of Radiology.* 2005; **78**: 533–537.

[41] Price SJ, Jena R, Burnet NG, Hutchinson PJ, Dean AF, Pena A, Pickard JD, Carpenter TA, Gillard JH, Improved delineation of glioma margins and regions of infiltration with the use of diffusion tensor imaging: An image-guided biopsy study. *American Journal of Neuroradiology.* 2006; **27**: 1969–1974.

[42] Di Costanzo A, Scarabino T, Trojsi F, Giannatempo GM, Popolizio T, Catapano D, Bonavita S, Maggialetti N, Tosetti M, Salvolini U, d'Angelo VA, Tedeschi G, Multiparametric 3T MR approach to the assessment of cerebral gliomas: tumor extent and malignancy. *Neuroradiology.* 2006; **48**: 622–631.

[43] Cha S, Lupo JM, Chen M-H, Lamborn KR, McDermott MW, Berger MS, Nelson SJ, Dillon WP, Differentiation of glioblastoma multiforme and single brain metastasis by peak height and percentage of signal intensity recovery derived from dynamic susceptibility-weighted contrast-enhanced perfusion mr imaging. *American Journal of Neuroradiology.* 2007; **28**: 1078–1084.

[44] Wang W, Steward CE, Desmond PM, Diffusion tensor imaging in glioblastoma multiforme and brain metastases: the role of p, q, L, and fractional anisotropy. *American Journal of Neuroradiology.* 2008; **30**: 203–208.

[45] Wang S, Kim S, Chawla S, Wolf RL, Zhang W-G, O'Rourke DM, Judy KD, Melhem ER, Poptani H, Differentiation between glioblastomas and solitary brain metastases using diffusion tensor imaging. *Neuroimage.* 2009; **44**: 653–660.

Captions of tables

Table 1: Pathology (primary tumour location), age and sex for 10 patients.

Table 2: Mean and standard deviation of choline-to-creatine (Cho/Cr) and choline-to-N-acetylaspartate (Cho/NAA) ratio in enhancing tumour, peri-enhancing area and non-enhancing/non-T2 hyperintense region for glioblastomas (GBM) and metastases (MET). The ratios are higher in the enhancing tumour and peri-enhancing region for glioblastomas compared to metastases.

Table 1

Case	Pathology (primary tumour location)	Age	Sex
1	glioblastoma multiforme (·)	71	female
2	glioblastoma multiforme (·)	64	male
3	glioblastoma multiforme (·)	64	male
4	glioblastoma multiforme (·)	58	male
5	glioblastoma multiforme (·)	62	male
6	metastasis (unknown)	50	male
7	metastasis (colon)	46	male
8	metastasis (lung)	51	male
9	metastasis (breast)	54	female
10	metastasis (unknown)	56	female

Table 2

		Non-enhancing/non-T2 hyperintense	Peri-enhancing	Enhancing tumour
Cho/Cr	GBM	1.42±0.19	2.02±0.73	3.13±1.22
	MET	1.28±0.18	1.18±0.15	1.80±0.24
Cho/NAA	GBM	0.48±0.06	1.08±0.89	2.39±2.05
	MET	0.43±0.08	0.54±0.08	0.97±0.13

Captions of figures

Figure 1: Left: the difference between the averaged choline-to-creatine ratio from the enhancing tumour and the non-enhancing/non-T2 hyperintense area for each patient. The dashed line illustrates the clear separation of metastases (MET) and glioblastomas (GBM). The average was 1.71 in glioblastomas and 0.51 in metastases. Right: the difference between the averaged choline-to-N-acetylaspartate ratio from the enhancing tumour and the non-enhancing/non-T2 hyperintense area for each patient. The dashed line illustrates the clear separation of metastases (MET) and glioblastomas (GBM). The average was 1.91 in glioblastomas and 0.54 in metastases.

Figure 2: Case 3 with a glioblastoma tumour. Top row: T2-weighted images of neighboring slices contained in the 2D-TSI box. Middle row: T2-weighted images with superimposed choline-to-N-acetylaspartate threshold result. Red and blue colors refer to abnormal and normal choline-to-N-acetylaspartate levels, respectively. Bottom row: MR spectra from voxels that are indicated on the grid of the middle MRI slice. MR spectrum (a) corresponds to a voxel that is situated in the adjacent tissue in the contralateral hemisphere. Choline is increased compared to N-acetylaspartate and creatine, suggesting tumour infiltration. MR spectra from normal (spectrum (b)) and tumour (spectrum (c)) tissue are also represented.

Figure 3: Case 4 with a glioblastoma tumour. Top row: T2-weighted images of neighboring slices contained in the 2D-TSI box. Middle row: T2-weighted images with superimposed choline-to-N-acetylaspartate threshold result. Bottom row: MR spectra from voxels that are indicated on the grid of the middle MRI slice. MR spectrum (b) shows increased choline with respect to N-

acetylaspartate and creatine, indicating tumour infiltration. MR spectra from the normal contralateral brain (spectrum (a)) and tumour tissue (spectrum (c)) are also depicted.

Figure 4: Case 6 with a metastasis tumour. Top row: T2-weighted images of neighboring slices contained in the 2D-TSI box. Middle row: T2-weighted images with superimposed choline-to-N-acetylaspartate threshold result. The red voxels completely fall inside the hyperintense area on the T2-weighted MR images. Bottom row: various MR spectra, located outside the tumoural lesion, in peri-enhancing edema or in normal brain parenchyma. Choline and creatine levels are similar, while N-acetylaspartate is increased, indicating no infiltration.

Figure 5: Case 10 with a metastasis tumour. Top row: T2-weighted images of neighboring slices contained in the 2D-TSI box. Middle row: T2-weighted images with superimposed choline-to-N-acetylaspartate threshold result. The red voxels completely fall inside the hyperintense area on the T2-weighted MR images. Bottom row: MR spectra showing increased N-acetylaspartate with similar choline and creatine peaks; no infiltration is detected.

Figure 6: Case 1 with a glioblastoma tumour. Top row: T2-weighted images of neighboring slices contained in the 2D-TSI box. Middle row: T2-weighted images with superimposed nosologic image. Abnormal tissue from MRI is indicated in red. Voxels that contain abnormal choline-to-N-acetylaspartate levels and fall outside the abnormal area on T2, are colored in white. Bottom row: MR spectra from voxels that are indicated on the nosologic image of the middle MRI slice. Voxels (a) and (b) are positioned in the white, infiltrated, area. The MR spectra show increased choline with respect to N-acetylaspartate and

creatine. Voxel (c) is situated inside the tumour.

Figure 7: Case 2 with a glioblastoma tumour. Top row: T2-weighted images of neighboring slices contained in the 2D-TSI box. Middle row: T2-weighted images with superimposed nosologic image. Abnormal tissue from MRI is indicated in red, green represents CSF, light blue white matter and dark blue gray matter. Voxels that contain abnormal choline-to-N-acetylaspartate levels and fall outside the abnormal area on T2, are colored in white. Bottom row: MR spectra from voxels that are indicated on the nosologic image of the middle MRI slice. MR spectrum (a) originates from tumour tissue while MR spectrum (b) originates from an infiltrated voxel, showing increased choline with respect to creatine and a higher choline-to-N-acetylaspartate ratio. MR spectrum (c) represents normal tissue.

Figure 8: Case 9 with a metastasis tumour. Top row: T2-weighted images of neighboring slices contained in the 2D-TSI box. Middle row: T2-weighted images with superimposed nosologic image. Bottom row: MR spectra from voxels, located at the tumour border, are indicated on the nosologic image of the middle MRI slice. No infiltration is detected.

Figure 9: Case 8 with a metastasis tumour. Top row: T2-weighted images of neighboring slices contained in the 2D-TSI box. Middle row: T2-weighted images with superimposed nosologic image. Bottom row: MR spectra from voxels, that are indicated on the nosologic image of the middle MRI slice. No infiltration is detected.

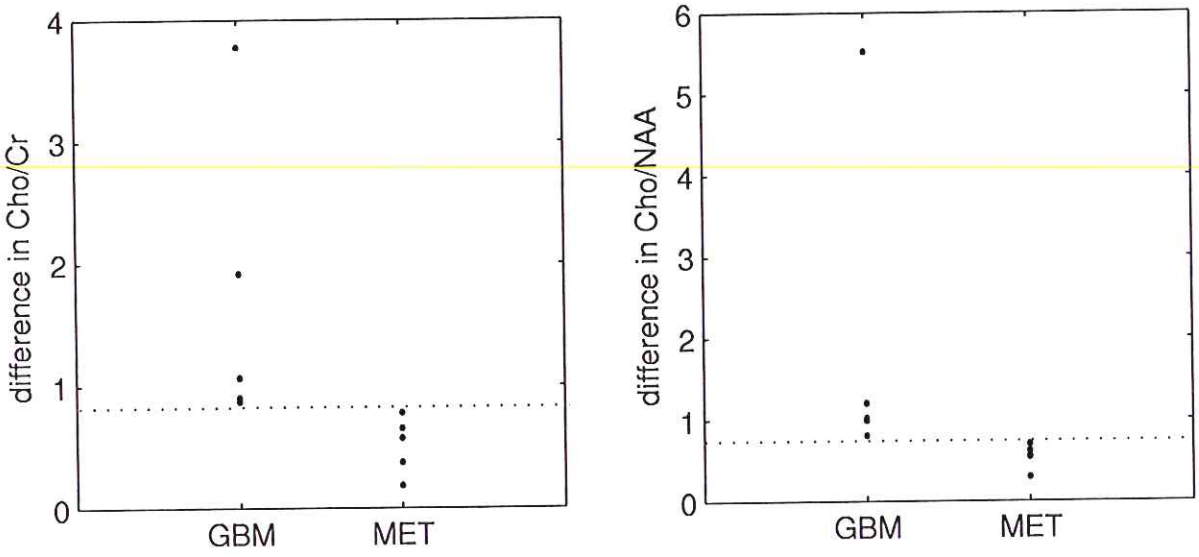

Fig. 1. Luts *et al.*

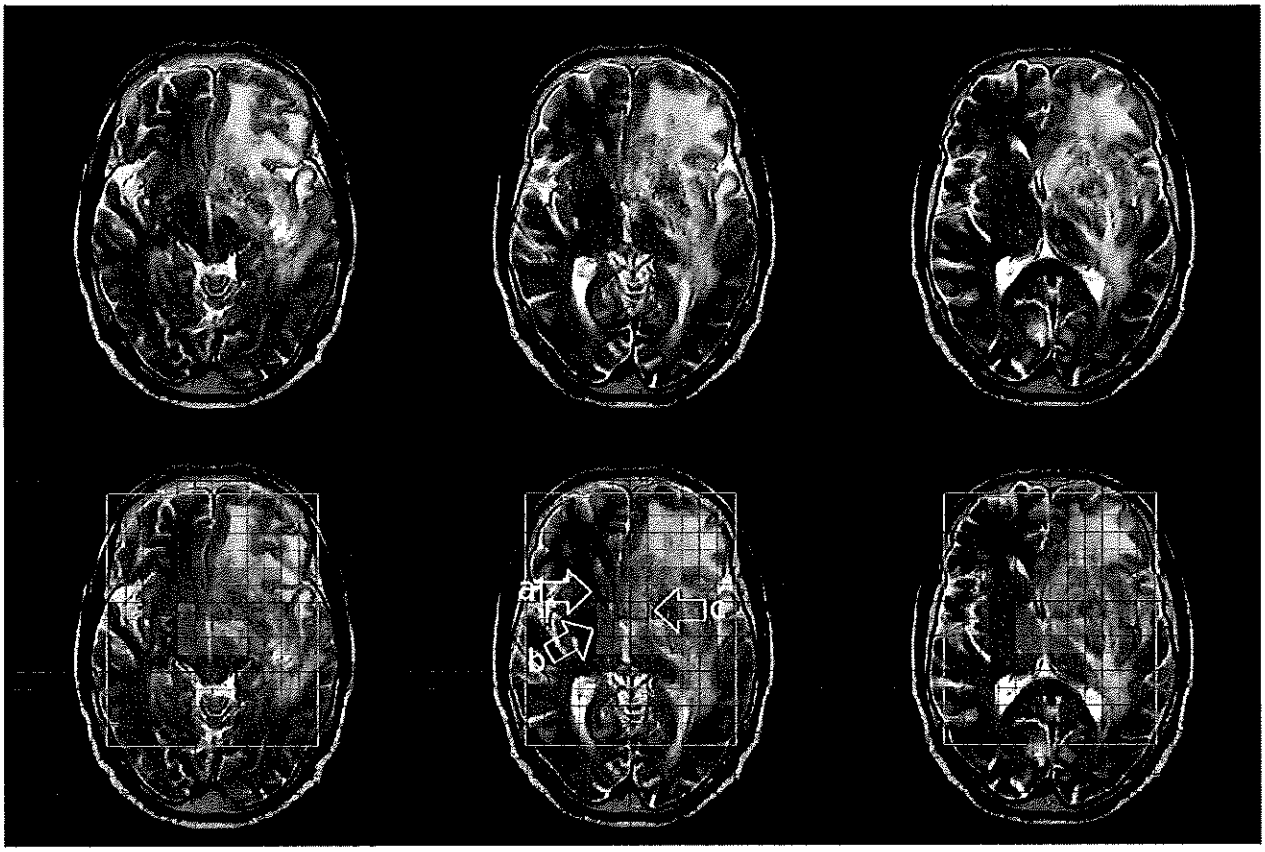

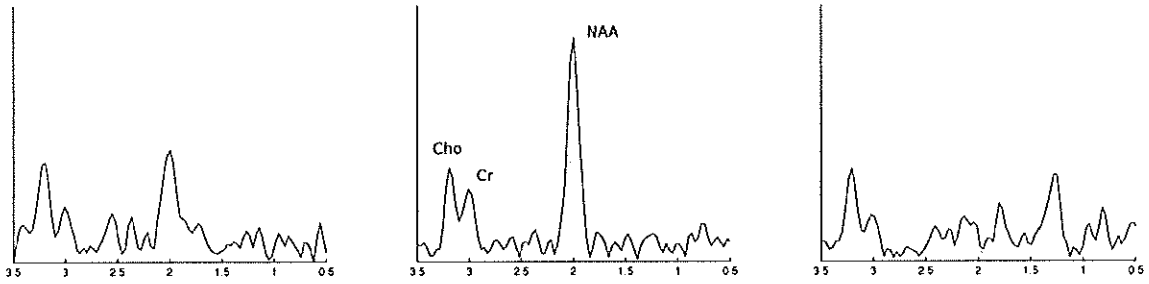

(a) (b) (c)

Fig. 2. Luts *et al.*

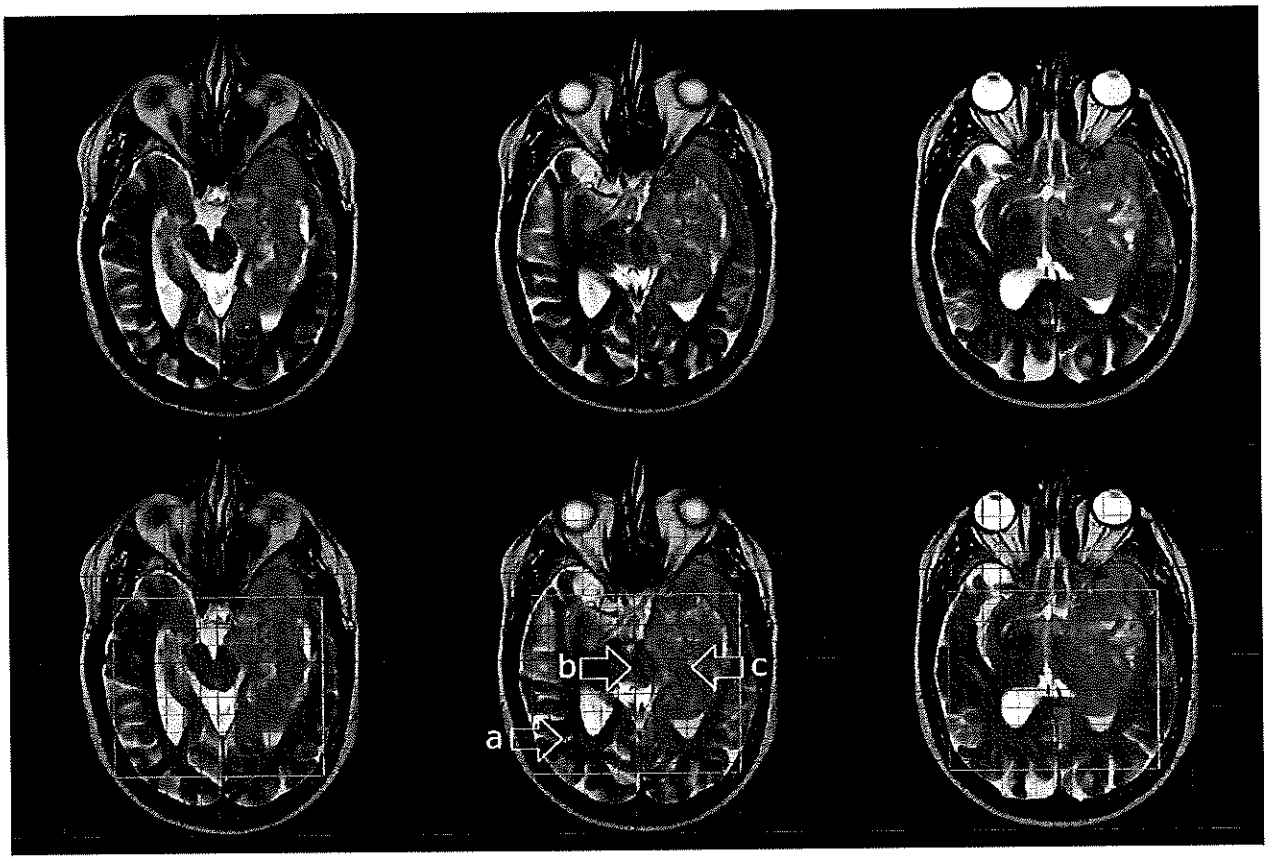

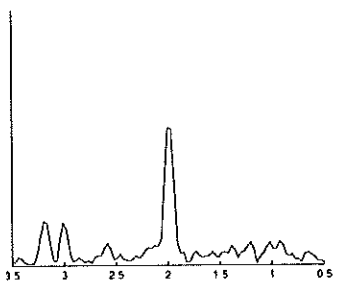

(a)

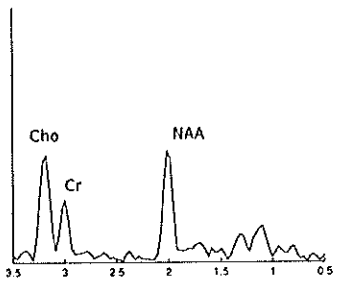

(b)

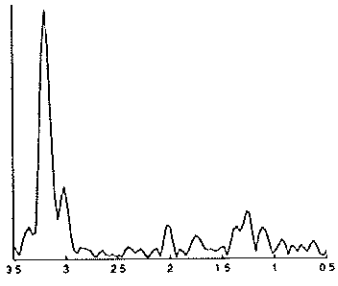

(c)

Fig. 3. Luts *et al.*

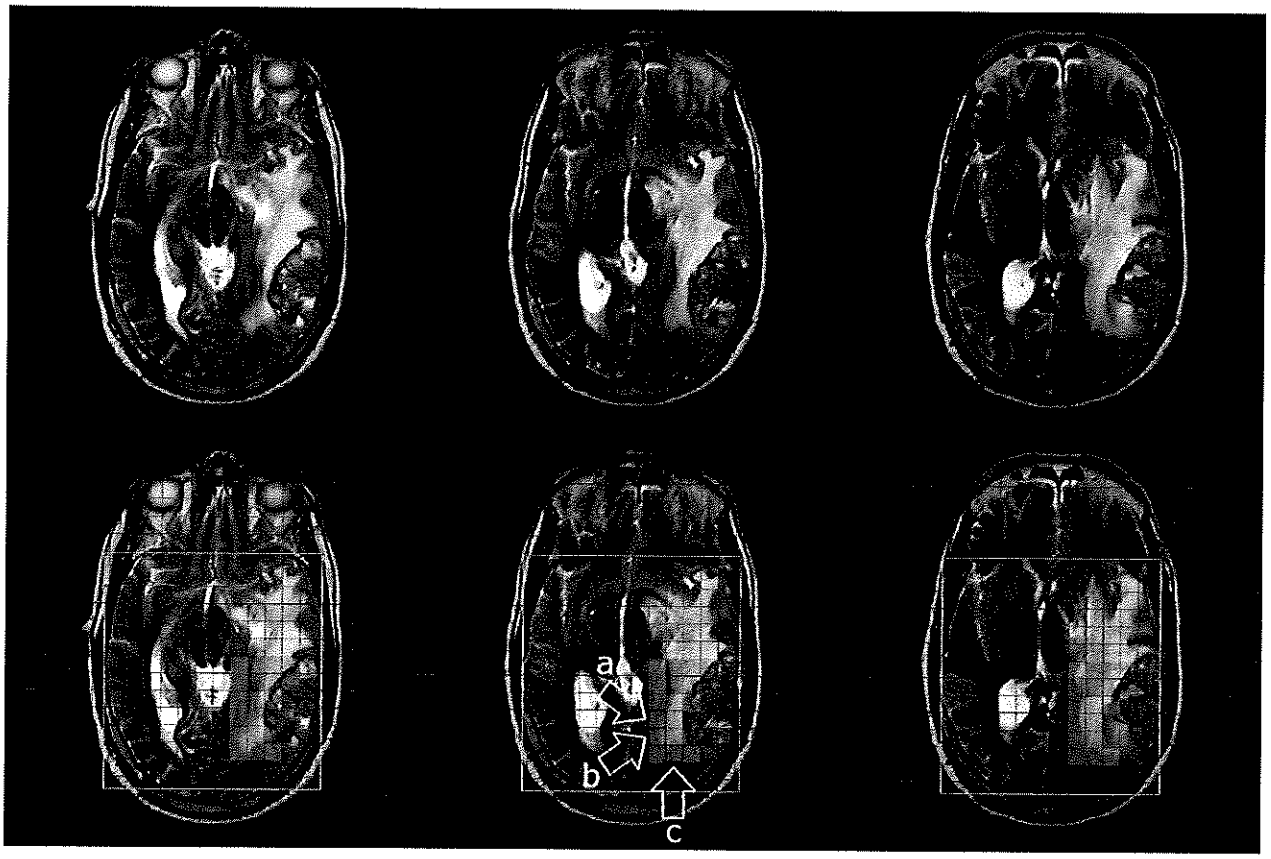

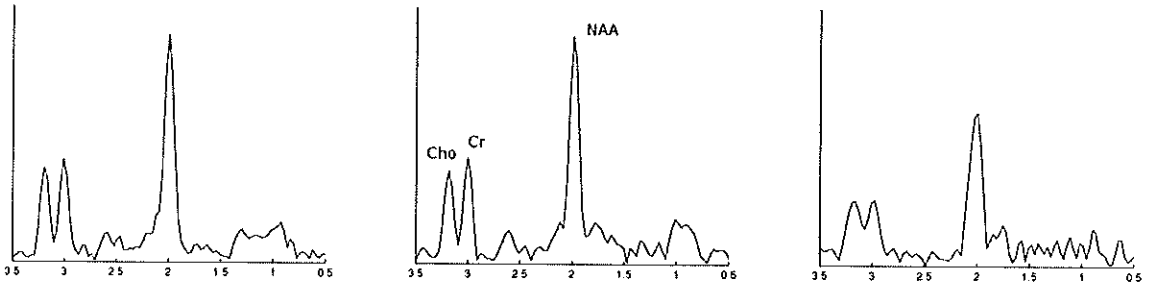

(a) (b) (c)

Fig. 4. Luts *et al.*

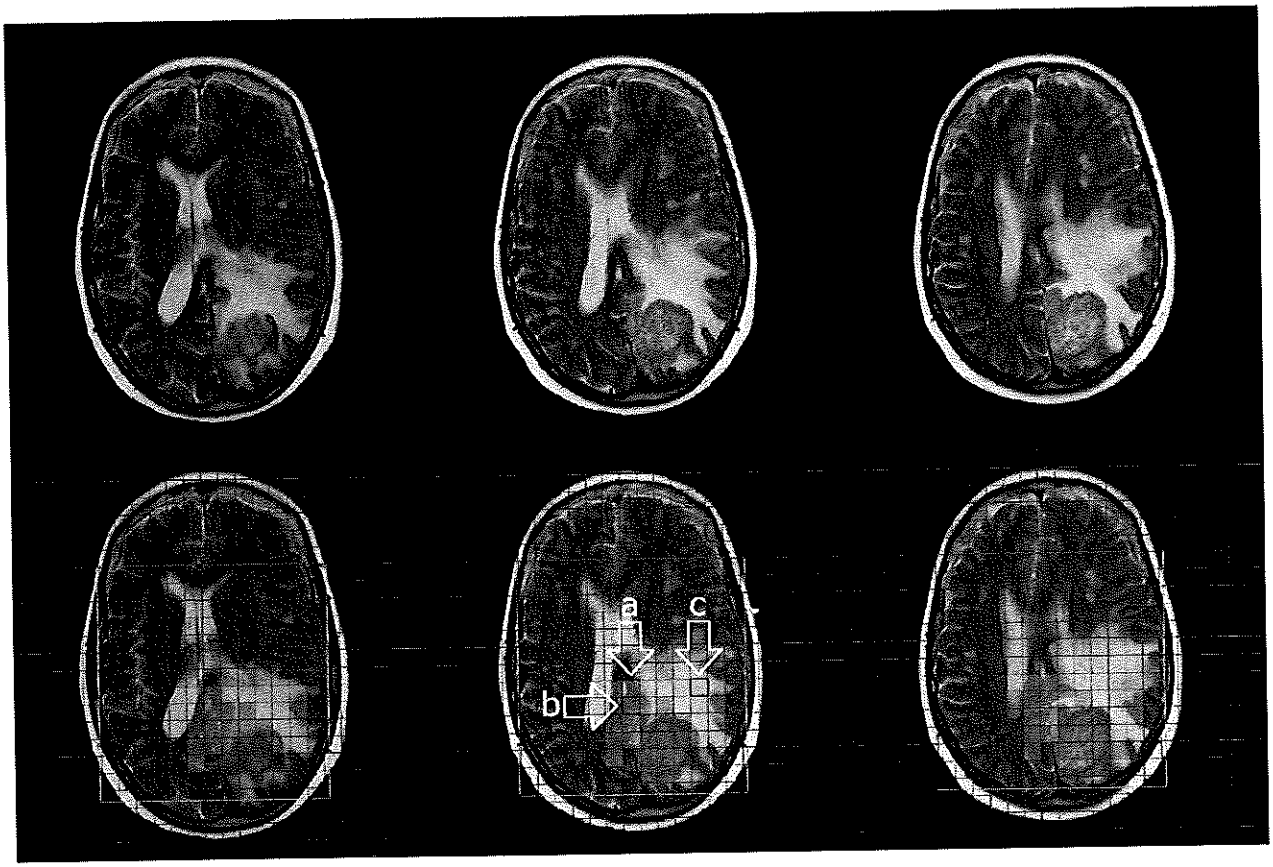

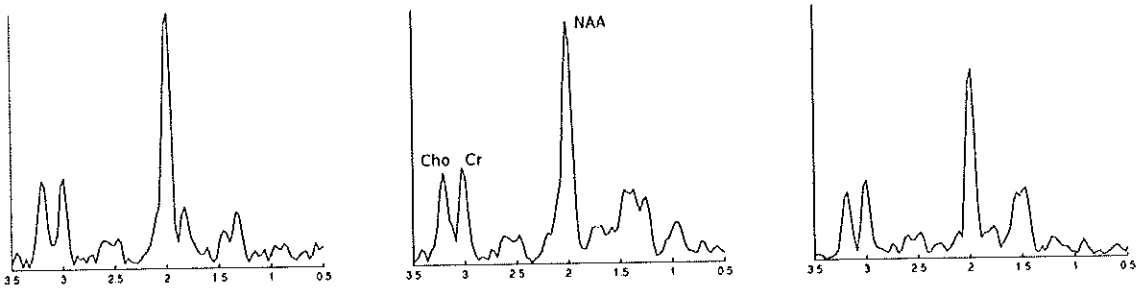

(a) (b) (c)

Fig. 5. Luts *et al.*

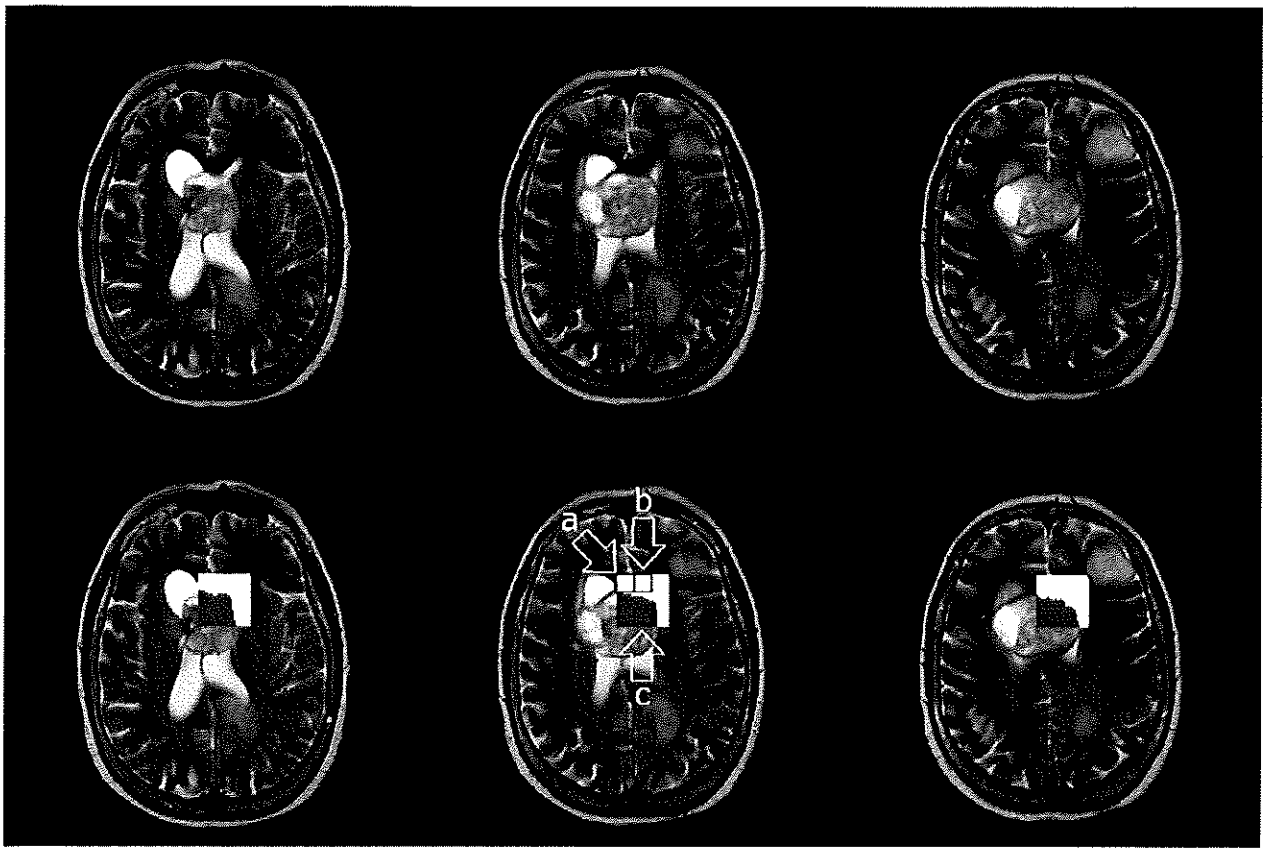

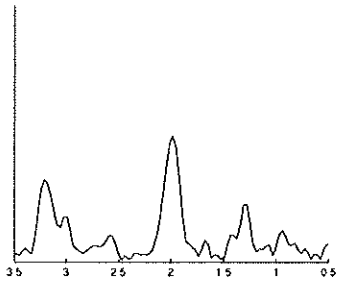

(a)

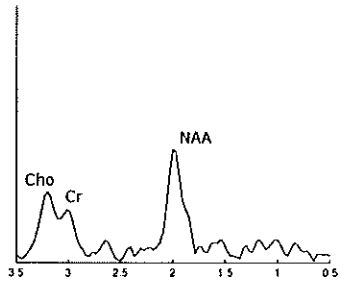

(b)

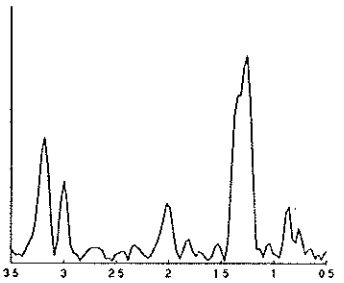

(c)

Fig. 6. Luts *et al.*

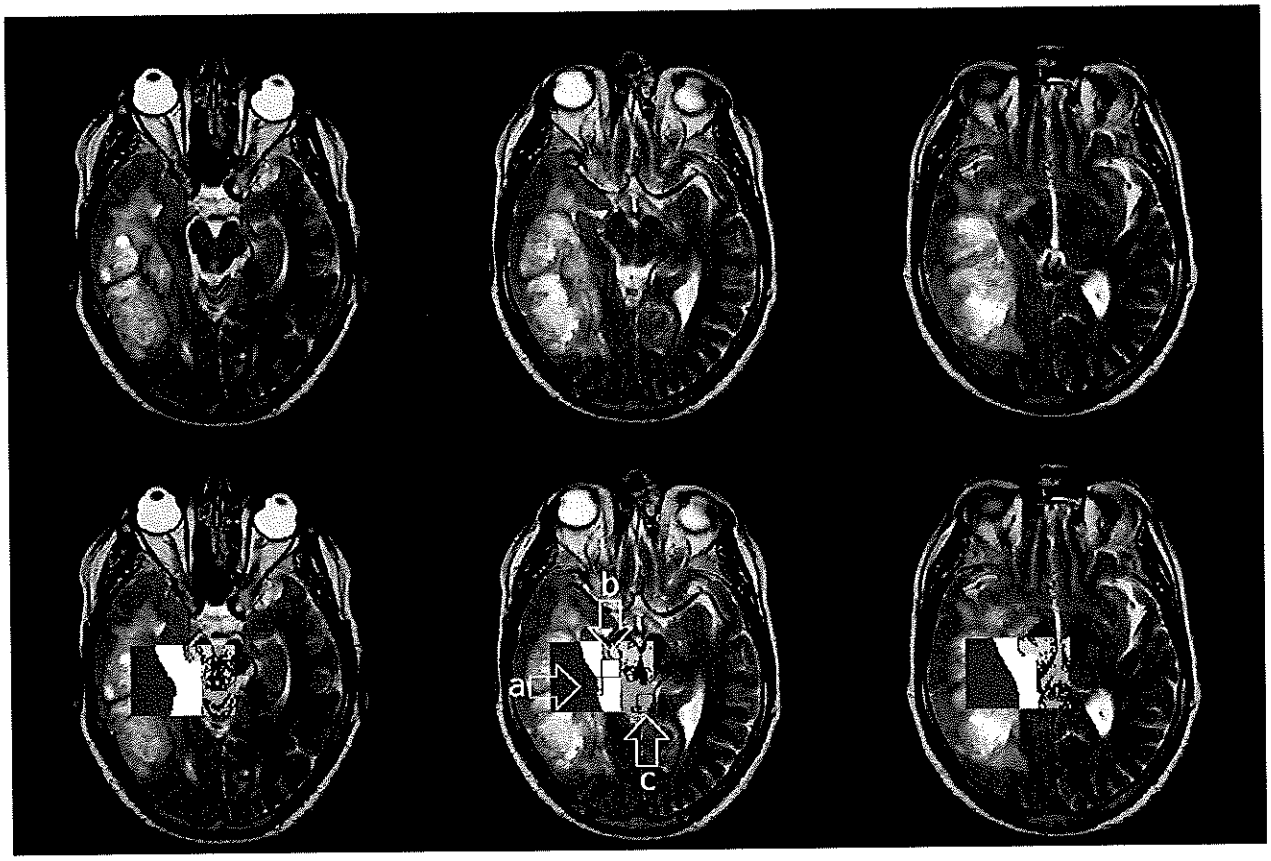

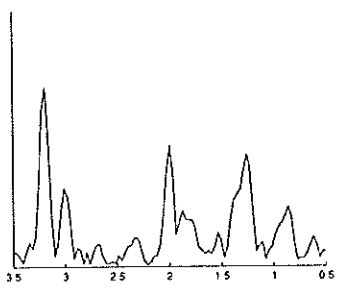

(a)

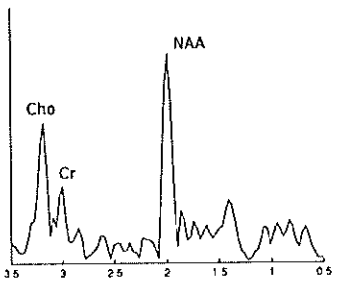

(b)

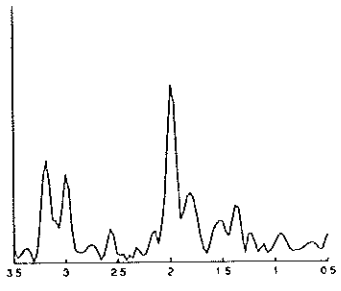

(c)

Fig. 7. Luts *et al.*

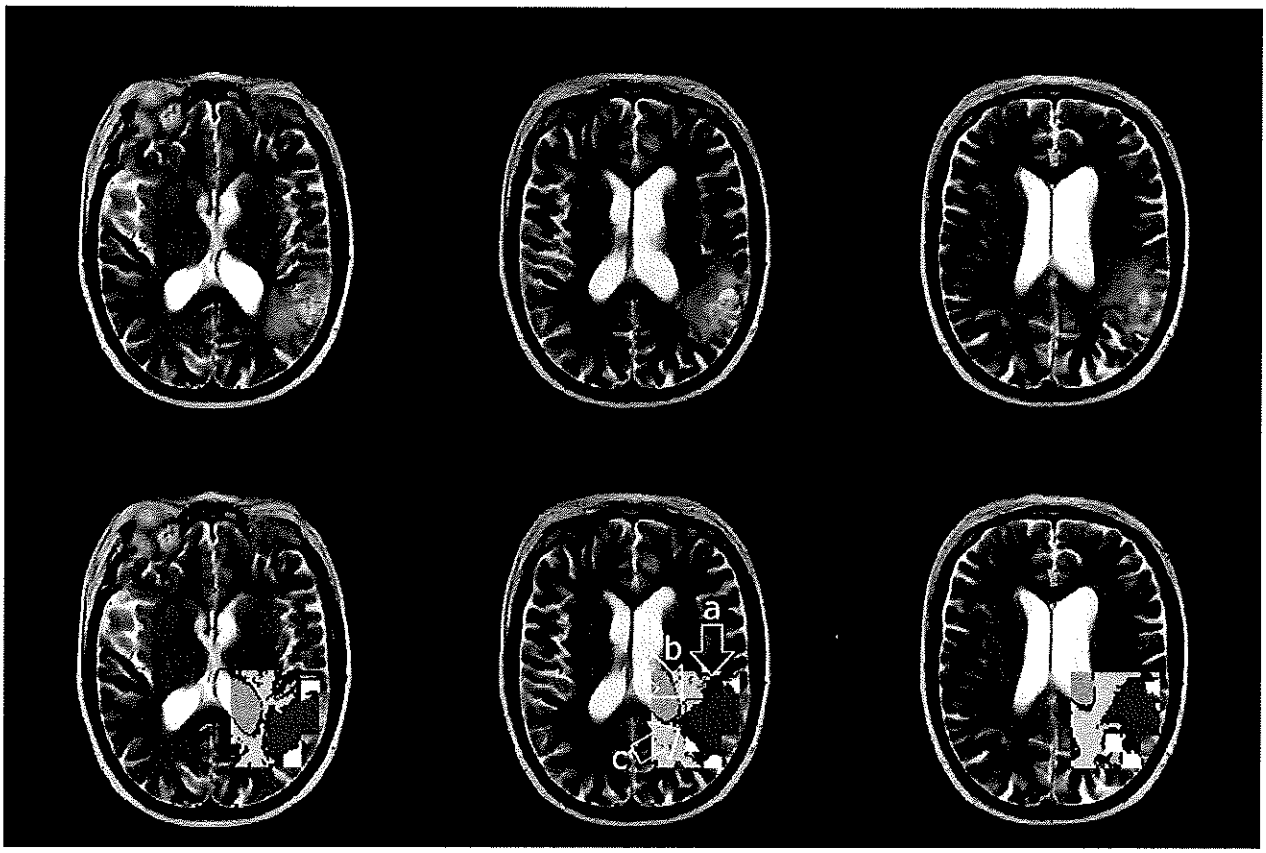

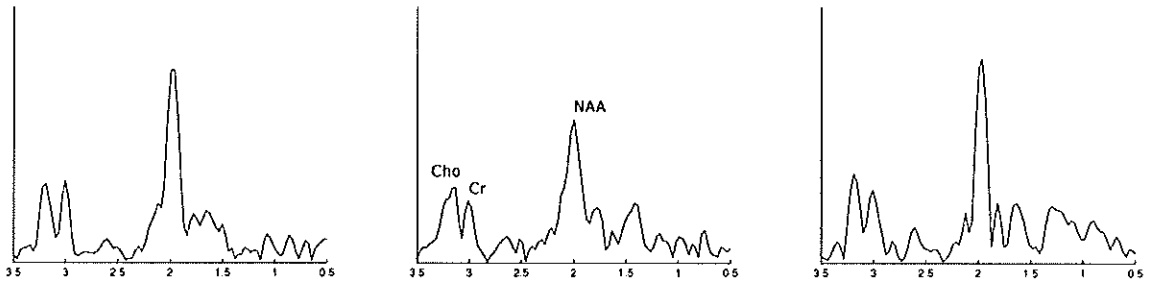

(a) (b) (c)

Fig. 8. Luts *et al.*

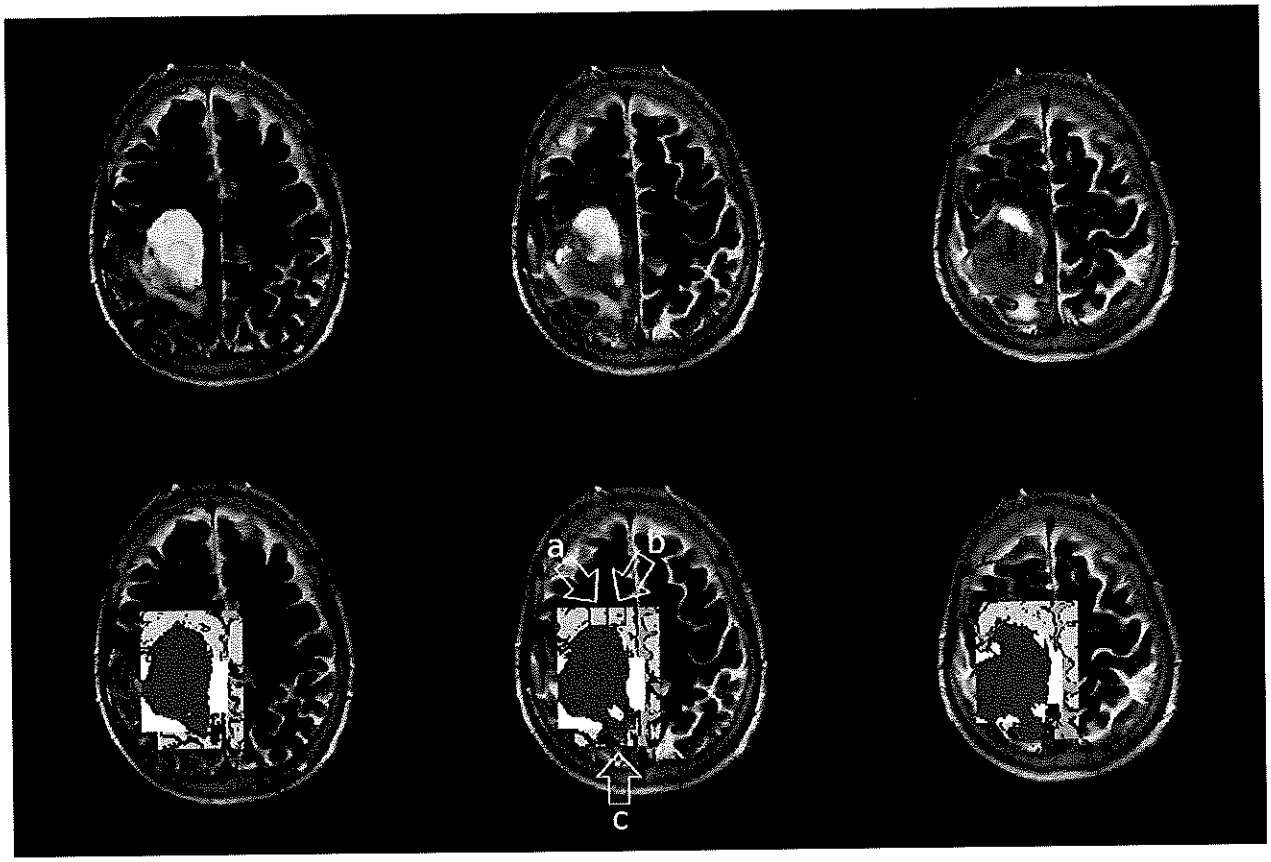

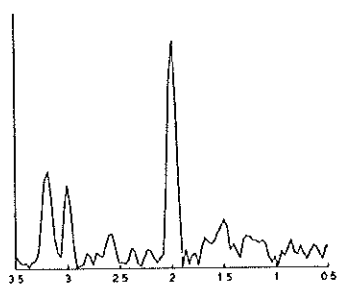

(a)

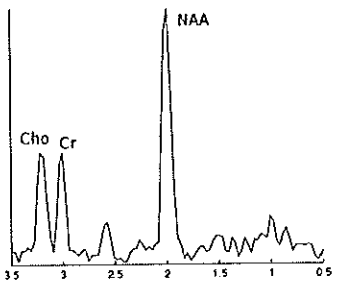

(b)

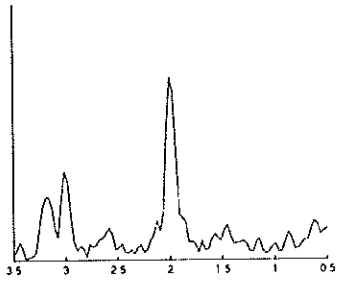

(c)

Fig. 9. Luts *et al.*